Innovative Model for Flow Governed Solid Motion based on Penalization and Aerodynamic Forces and Moments

Héloïse Beaugendre, François Morency

Innovative Model for Flow Governed Solid Motion based on Penalization and Aerodynamic Forces and Moments

Héloïse Beaugendre, François Morency

Innovative Model for Flow Governed Solid Motion based on Penalization and Aerodynamic Forces and Moments

Héloïse Beaugendre[*], François Morency[†]

Project-Team CARDAMON

Abstract: This work proposes a fluid-solid interaction model. It is formulated for a laminar flow modeled by the incompressible Navier-Stokes equations in which we consider the presence of a rigid moving solid. The model is formulated inside an immersed boundary method based on a penalization technique. The penalization technique imposes the body effects on the flow. The velocity field is extended inside the solid region and a penalty term enforces the rigid motion inside the solid region. This technique offers a great flexibility to modify the geometry of the solid. The forces and angular momentum needed for the fluid-solid interaction model are computed with an innovative method suitable for the penalized equations method. The method is validated successfully for an oscillating airfoil in large flapping motion. Effects of different geometries on aerodynamic coefficients can then be explored. The fluid-solid interaction model is also verified for solid motions governed by the flow, such as falling cylinder and plate.

Key-words: Penalization, IBM, Aerodynamic forces and moments computation, VIC scheme, Oscillating-airfoil, Fluid-solid interaction

This is a note

This is a second note

[*] Univ. Bordeaux, IMB, UMR 5251, F-33400, Talence, France; CNRS, IMB, UMR 5251, F-33400, Talence, France; Bordeaux INP, IMB, UMR 5251, F-33400,Talence, France; INRIA, F-33400 Talence, France.
[†] TFT Laboratory, Département de génie mécanique, École de Technologie Supérieure, Montréal, Canada

Modèle novateur pour le mouvement d'un solide entraîné par l'écoulement basé sur la pénalisation et le calcul des forces et moments aérodynamiques

Résumé : La méthode d'interaction fluide-solide proposée dans ce rapport est formulée pour un écoulement laminaire. L'écoulement est modélisé par les équations de Navier-Stokes incompressibles modifiées, dans lesquelles nous considérons la présence d'un corps rigide en mouvement. Le modèle est formulé dans le cadre d'une méthode de frontières immergées basée sur une technique de pénalisation pour tenir compte du corps. Le champ de vitesse est étendu dans la région du corps rigide et un terme de pénalisation impose le mouvement rigide à l'intérieur du solide. Cette technique offre une grande souplesse pour modifier la géométrie du corps. Une méthode innovante appropriée pour le calcul des forces et des moments angulaires basée sur les équations pénalisées est proposée et validée pour une aile oscillante dans un grand mouvement de battement. Les effets de différentes géométries peuvent ensuite être explorés. Le modèle d'interaction fluide-solide est aussi vérifié pour des mouvements de solides gouvernés par l'écoulement, comme le cas d'un cylindre ou d'une plaque en chute libre.

1   Introduction

The goal of most external flow analysis in engineering is the evaluation of aerodynamic forces and moments. For complex flows, with massive separations for example, computational fluid dynamics (CFD) is often the only way to reach this goal. CFD simulations are usually performed using two types of grids: body-fitted grids and embedded grids. For body-fitted grids, external mesh faces match up with the body surfaces and external boundary faces. On the contrary, flow simulations by immersed boundary methods (IBM) use a grid that does not fit the body geometry, thus avoiding most of the difficulties associated with grid generation. IBMs can easily model flows around complex geometries in large motion [1] and are well suited for simulating complex fluid-solid interactions. The Cartesian grid, most widely used with the IBM, limits the application to Euler or Laminar flow, unless a local grid refinement strategy [2] or a specific turbulent wall model is used [3]. Methodological advances on IBM allow the simulation of compressible flows at high Reynolds numbers [4] and therefore enable its use for aeronautic applications, such as computation of droplet impingement [5].

As discussed by Mittal *et al.* in [1] and most recently by Sotiropoulos *et al.* in [6], IBMs can be classified into two categories: sharp interface methods and diffused interface methods. In the first category the presence of boundaries is taken into account at the discrete level. The goal is to insure properties conservation closed to the boundaries and improve the accuracy at the interface. The ghost-cell approach [4, 7, 8] belongs to this category and uses, at ghost points, values that are extrapolated from the fluid to impose the appropriate boundary conditions at the interface. The sub-mesh penalty method [9], the immersed interface method [10] and the cut-cell method [11] are other approaches belonging to this class. In the second category, the diffused interface methods avoid the difficulties associated to the accurate tracking of the fluid-solid interface position. The presence of boundaries is modeled by adding a continuous forcing term directly to the flow equations. Immersed nodes exert a force in the momentum equations. The effect of immersed boundaries is distributed on surrounding nodes using delta or mask functions. Penalization method [12, 13] and its recent developments [14, 15, 16] belongs to this category. With penalization, solid bodies are represented as porous media with a very small permeability [17].

In this paper, we propose to extend the use of an IBM that combines the advantage of the penalization and of the Vortex-in-Cell (VIC) methods [18]. The vorticity field can be seen as the signature of bluff bodies flows. Therefore, a vorticity formulation of the Navier-Stokes equations may appear as the natural framework to study these flows. Since the advection of vorticity is predominant for moderate and high Reynolds number, Lagrangian or semi-Lagrangian schemes are suitable to discretize such equations. Particle methods and VIC methods belong to this kind of approaches. Particle methods have long been used to compute vortex flows [19, 20, 21, 22]. The difficulties of such methods rely on a delicate tuning of the velocity boundary conditions especially for complex geometries. In such sense, immersed boundary methods and especially, penalization, simplify the treatment of boundary conditions [23, 24, 25, 26]. Active research is performed on such methods to improve their accuracy [27, 28], to increase the range of applications and physical flows modelled [29], and to remain competitive in terms of computing performances [30].

It is well known that the fluid interacts with the solid through pressure and viscous stress at the wall. However, for vorticity-based numerical simulation, the pressure distribution is not known. The forces can be computed from the velocity and vorticity following the method pro-

posed by Noca *et al.* [31], as done by Ploumhans *et al.* [20]. Recently, some authors have expressed some doubt about the validity of the forces predicted by this method for unsteady flows when pressure and vorticity are not uniform at infinity [32]. Moreover, for vortex flow formulation, the method does not allow the computation of moments on rigid body. Eldredge [33] proposes a method to compute both forces and moment on body, based on integration along the surface of the vorticity derivative in the normal direction. For penalization, this method is not easy to apply because the vorticity is not defined at the surface but rather at cartesian grid points near the surface. Instead, we propose an innovative forces and moment computational method based on the global momentum change and angular momentum change inside the body.

The first specific objective of this paper is to propose a mathematical model for the fuid-solid interactions within IBM. The second objective is to validate the forces and momentum calculations within the VIC-IBM scheme using static and moving bodies. The flexibility offered by the use of IBM and the level-set description of the geometries are then demonstrated. IBMs are well suited for parametric study of geometry effects on the flow because no remeshing is needed when the geometry is modified [34]. The third objective is to verify the fluid-solid interaction model. This is done by using IBMs for the computation of flow induced body motions, such as the free fall of a solid in a fluid [35, 36, 37]. IBMs are particularly attractive to study motion of non spherical bodies, such as the autorotation of flat plate [38, 39].

The paper is organized as follows, first, the penalized Navier-Stokes equations are presented in section 2, together with the numerical method based on a VIC scheme. The new model used to compute the forces and moment exerted by a fluid on a solid body is proposed in section 3, along with appropriate governing equations for fluid-solid interactions. In the fourth section, test cases are presented to validate forces and moments computations against literature results and examples of fluid-solid interactions are presented.

2   Penalized Navier-Stokes equations and VIC scheme

2.1   Physical model

The fluid-solid interaction flow model proposed in this work is based on an incompressible laminar Newtonian flow around a body considered as rigid (without any deformation) and delimited by level-set functions. The mass and momentum conservation equations are

$$\nabla \cdot \mathbf{u} = 0 \quad \text{in} \ \ \Omega \tag{1a}$$

$$\frac{\partial \mathbf{u}}{\partial t} + (\mathbf{u} \cdot \nabla)\,\mathbf{u} - \nu\nabla^2\mathbf{u} + \frac{1}{\rho}\nabla p = 0 \quad \text{in} \ \ \Omega. \tag{1b}$$

where $\mathbf{u}$ is the velocity vector, $\nu = \mu/\rho$ is the kinematic viscosity, ρ is the density, and p is the pressure. Now we consider, in Ω, the presence of a rigid moving solid S^i. The boundary of S^i is computed from a level set function Φ_{s^i}. Φ_{s^i} is the signed distance function to S^i, typically Φ_{s^i} will be negative inside the object and positive outside, see figure 1 for an illustration of the signed distance function, embedded into a Cartesian grid, corresponding to a wing and an ice debris.

The penalization technique extends the velocity field inside the solid body, as illustrated in figure (2), and solve the flow equations with a penalty term to enforce rigid motion inside the solid as proposed by [24]. Let $\mathbf{u}_{s^i}$ be the rigid moving body velocity vector of S^i. Inside S^i, the momentum equation becomes $\mathbf{u} = \mathbf{u}_{s^i}$ and remains equation (1b) outside S^i.
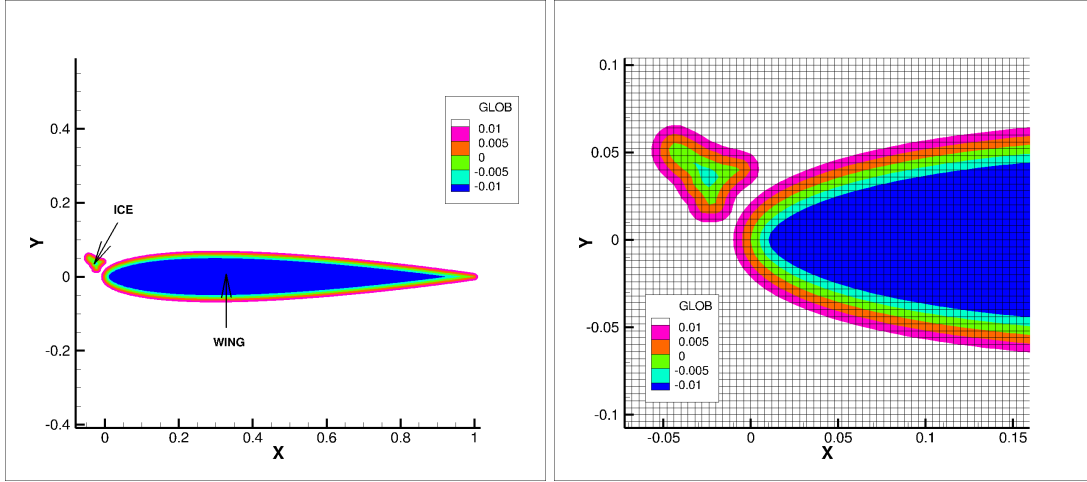
Figure 1: Global level-set function of two rigid bodies (wing and ice debris) computed onto a Cartesian grid.

This is summarized as follows: given a very large penalization parameter, $\lambda \gg 1$, and denoting by χ_{s^i} the characteristic function of the solid S^i, *i.e.* $\chi_{s^i} = 1$ inside S^i and $\chi_{s^i} = 0$ outside S^i, the penalized Navier-Stokes equations are

$$\frac{\partial \mathbf{u}}{\partial t} + (\mathbf{u} \cdot \nabla)\,\mathbf{u} - \nu\nabla^2\mathbf{u} + \frac{1}{\rho}\nabla p = \lambda\chi_{s^i}(\mathbf{u}_{s^i} - \mathbf{u}) \qquad \text{for } \mathbf{x} \in \Omega \text{ and } t > 0, \tag{2}$$

coupled with the incompressible mass conservation (1a). This model can easily be generalized to multiple rigid bodies S^i.

To solve our governing equations the following strategies have been chosen:

1. A vortex formulation of our governing equations is used: this formulation is especially well adapted to study oscillatory motions that create large flow separation around aerodynamic bodies.

2. A vortex in cell (VIC) scheme is used to solve the obtained equations: this scheme offers less CFL restrictions than classical schemes.

3. A time splitting algorithm allows to take into account the specific requirement of each equation term, for example the implicit treatment of the penalization term for accuracy purpose.

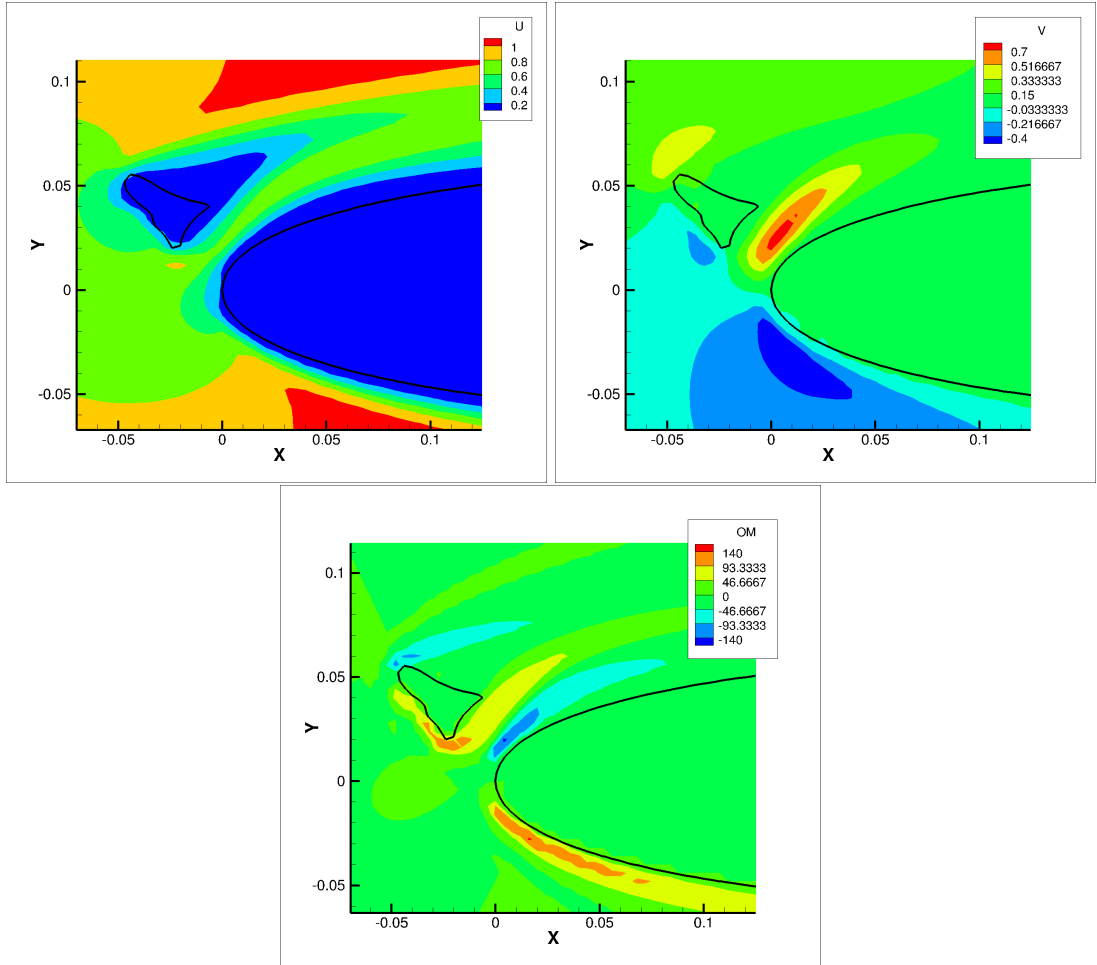Let us give more precision on each choice previously described.

Figure 2: Penalization technique, the flow field is extended inside the bodies, u component of the velocity, v component of the velocity and vorticity.

2.2 Vortex formulation

Let us consider the penalized Navier-Stokes equation in the vorticity formulation by applying the **curl** operator to equation (2), with $\boldsymbol{\omega} = \nabla \times \mathbf{u}$ in Ω

$$\frac{\partial \boldsymbol{\omega}}{\partial t} + (\mathbf{u} \cdot \nabla)\,\boldsymbol{\omega} \;\; = \;\; (\boldsymbol{\omega} \cdot \nabla)\,\mathbf{u} + \nu\nabla^2\boldsymbol{\omega} + \lambda\nabla \times [H(\Phi_{s^i})(\mathbf{u}_{s^i} - \mathbf{u})] \tag{3}$$

$$\text{with} \quad \nabla \cdot \mathbf{u} \;\; = \;\; 0 \quad \text{in } \Omega. \tag{4}$$

In equation (3), $\chi_{s^i} = H(\Phi_{s^i})$, where H is the Heaviside function. In this paper, the vorticity field is numerically determined by a particle discretization using the scheme presented in the next section. Because the equations are not written in primitive variables, special treatments are needed to recover the velocity field and to impose the boundary conditions. Since the incompressible velocity field is divergence-free, from the vector field theory, we can define a vector potential $\boldsymbol{\Psi}$ such that

$$\mathbf{u} = \nabla \times \boldsymbol{\Psi}. \tag{5}$$

This potential vector is imposed to be solenoidal, that is $\nabla \cdot \boldsymbol{\Psi} = 0$, and given $\boldsymbol{\omega}$ the updated vorticity field, the stream function field is computed by solving the linear Poisson equation,

$$\Delta\boldsymbol{\Psi} = -\boldsymbol{\omega}, \tag{6}$$

on the cartesian grid with boundary conditions on $\partial\Omega$, using a Fast Fourier Transform (FFT) solver.

2.3 VIC scheme

The Vortex-In-Cell (VIC) scheme computes the non linear advection by tracking the trajectories of Lagrangian particles through a set of ODEs. An Eulerian grid is adopted to solve the velocity field, the diffusive term, and the penalization term. Given $D/Dt(\cdot)$, the material derivative, equation (3) becomes

$$\frac{D\boldsymbol{\omega}}{Dt} \;\; = \;\; (\boldsymbol{\omega} \cdot \nabla)\,\mathbf{u} + \nu\nabla^2\boldsymbol{\omega} + \lambda\nabla \times [H(\Phi_{s^i})(\mathbf{u}_{s^i} - \mathbf{u})] \tag{7}$$

The domain Ω is meshed using a uniform fixed cartesian grid. We denote the time step Δt, such that $t^n = n\Delta t$ and $\Phi_{s^i}^n$, $\mathbf{u}^n$, $\boldsymbol{\omega}^n$ are grid values of the level set functions, velocity, and vorticity. The vorticity field $\boldsymbol{\omega}$ is represented by a set of particles

$$\boldsymbol{\omega}(\mathbf{x}) = \sum_{p=1}^{N} v_p\boldsymbol{\omega}_p\zeta\left(\mathbf{x} - \mathbf{x}_p\right), \tag{8}$$

where N is the number of particles, $\mathbf{x}_p$ the particle location, v_p and $\boldsymbol{\omega}_p$ are the volume and the strength of a general particle p. ζ is a smooth distribution function, such that $\int \zeta(x)\,dx = 1$, which acts on the vortex support. In vortex methods, the rate of change of vorticity is modeled by means of discrete vortex particles, such that the solution of (7) is localized only in the rotational regions of the flow field. This is the most important advantage of the vortex methods, that is, the computational efforts are naturally addressed only to specific flow field zones.

2.4   Splitting algorithm

A viscous splitting algorithm solves the equation (3). Each time step Δt is solved using three sub-steps as follows.

$$1 - \text{Advection:} \qquad \frac{D\boldsymbol{\omega}}{Dt} = \frac{\partial \boldsymbol{\omega}}{\partial t} + (\mathbf{u} \cdot \nabla)\,\boldsymbol{\omega} = 0. \tag{9a}$$

$$2 - \text{Stretching and diffusion:} \qquad \frac{\partial \boldsymbol{\omega}}{\partial t} = (\boldsymbol{\omega} \cdot \nabla)\,\mathbf{u} + \nu\nabla^2\boldsymbol{\omega}. \tag{9b}$$

$$3 - \text{Penalization term:} \qquad \frac{\partial \boldsymbol{\omega}}{\partial t} = \lambda\nabla \times \left(H\left(\Phi_{s^i}\right)\left(\mathbf{u}_{s^i} - \mathbf{u}\right)\right). \tag{9c}$$

sub-step 1: advection

Starting with $\boldsymbol{\omega}^n$, grid vorticity above a certain cut-off value will create particles at grid point locations [40], figure 3 a). Then, using equation (9a), particles are displaced with a fourth order Runge-Kutta time-stepping scheme, figure 3 b). From the new vortex particles' location, the vorticity field is remeshed on the grid, $\omega^\star$, by the M_4' third order interpolation kernel introduced by [41], figure 3 c).
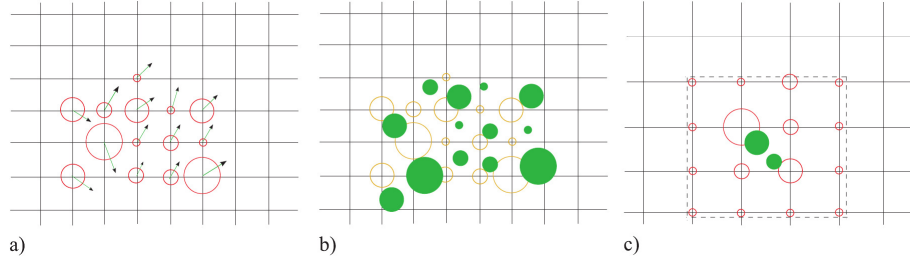

Figure 3: Particles interpolation scheme. The circle's size denotes the strenght of the particle and the solid circles represent the advected particles. a) vortex particles and velocity field; b) advection step; c) remesh-diffusion step.

sub-step 2: stretching and diffusion

The equation to solve for vortex stretching and viscous contribution is given by equation (9b) applied to $\omega^\star$. This equation is approximated onto the grid with an Euler explicit scheme, while the Laplacian is evaluated with a second order accurate standard five points stencil. The results is noted $\omega^{\star\star}$.

sub-step 3: penalization

The penalization term is evaluated using equation (9c). In our simulations, λ is fixed to $10^8/\Delta t$. An implicit Euler time discretization is used to approximate $\mathbf{u}^{n+1}$ in the penalization term:

$$\mathbf{u}^{n+1} = \frac{\mathbf{u}^{\star\star} + \lambda\Delta t H(\Phi_{s^i})\mathbf{u}_{s^i}^n}{1 + \lambda\Delta t H(\Phi_{s^i})}. \tag{10}$$

where $\mathbf{u}^{\star\star}$ is the velocity computed using $\boldsymbol{\omega}^{\star\star}$ resulting of sub-step 2 ($\Delta\boldsymbol{\Psi}^{\star\star} = -\boldsymbol{\omega}^{\star\star}$ and $\mathbf{u}^{\star\star} = \nabla \times \boldsymbol{\Psi}^{\star\star}$). The vorticity field at t^{n+1} is then evaluated on the grid by taking the **curl** of the velocity, $\boldsymbol{\omega}^{n+1} = \nabla \times \mathbf{u}^{n+1}$, and computing the derivative through the second order centered finite differences approximation. This method is unconditionally stable and enables to take a very large penalization parameter to insure accuracy.

3 Aerodynamic forces and moment computations and fluid-solid interaction model

The penalization term in equation (3), the last term on the right hand side, can also be considered as being the rigid body effect on fluid. At each time step, the penalization term forces the velocity inside the rigid body S^i to be equal to $\mathbf{u}_{s^i}$. In velocity formulation, the local momentum change imposed by the penalization is computed by

$$\frac{\partial u}{\partial t} = \lambda H(\Phi_{s^i})(\mathbf{u}_{s^i} - \mathbf{u}) \tag{11}$$

In our formulation, the velocity $\mathbf{u}$ is implicitly calculated by (10). Thus, the penalization term become

$$\frac{\partial u}{\partial t} = \lambda H(\Phi_{s^i}) \left(\mathbf{u}_{s^i}^n - \left(\frac{\mathbf{u}^{\star\star} + \lambda \Delta t H(\Phi_{s^i}) \mathbf{u}_{s^i}^n}{1 + \lambda \Delta t H(\Phi_{s^i})} \right) \right) \tag{12}$$

$$\frac{\partial u}{\partial t} = \lambda H(\Phi_{s^i}) \left(\frac{\mathbf{u}_{s^i}^n (1 + \lambda \Delta t H(\Phi_{s^i})) - (\mathbf{u}^{\star\star} + \lambda \Delta t H(\Phi_{s^i}) \mathbf{u}_{s^i}^n)}{1 + \lambda \Delta t H(\Phi_{s^i})} \right) \tag{13}$$

$$\frac{\partial u}{\partial t} = \lambda H(\Phi_{s^i}) \left(\frac{\mathbf{u}_{s^i}^n - \mathbf{u}^{\star\star}}{1 + \lambda \Delta t H(\Phi_{s^i})} \right). \tag{14}$$

The global momentum change is obtained by integration over the computational solid domain S^i and the forces are defined as

$$\mathbf{F} = \int_{S^i} \frac{\rho_f \lambda H(\Phi_{s^i})}{1 + \lambda \Delta t H(\Phi_{s^i})} (\mathbf{u}_{s^i}^n - \mathbf{u}^{\star\star}) d\mathbf{x}. \tag{15}$$

In a similar way, the angular momentum change created by the penalization term requires an integration over the solid domain S^i and the instantaneous pitching moment is defined by

$$\mathbf{T} = \int_{S^i} \frac{\rho_f \lambda H(\Phi_{s^i})}{1 + \lambda \Delta t H(\Phi_{s^i})} \mathbf{r} \times (\mathbf{u}_{s^i}^n - \mathbf{u}^{\star}) d\mathbf{x}. \tag{16}$$

In 2D flows, the drag, lift and pitching moment coefficients are defined respectively as

$$C_X = \frac{F_x}{1/2 \rho_f U_\infty^2 c} \qquad C_Y = \frac{F_y}{1/2 \rho_f U_\infty^2 c} \qquad C_m = \frac{T}{1/2 \rho_f U_\infty^2 c^2}. \tag{17}$$

where the x axis is aligned with the far field velocity vector U_∞, the y axis is perpendicular to the far field velocity vector and c is the airfoil chord. For an imposed motion of the solid S^i, given $\mathbf{u}_{s^i}$ we compute the aerodynamic coefficients given by equation (17).

The model for fluid-solid interaction is different from the one used in the previous paper [42]. For a fluid-solid interaction the forces acting on the solid S^i induce its motion, the governing equations are then given by

$$\frac{\partial \mathbf{u}_{s^i}}{\partial t} = \frac{\mathbf{F}}{Ma} + \frac{(\rho_{s^i} - \rho_f)}{\rho_{s^i}} \mathbf{G} \tag{18}$$

$$\frac{\partial \theta}{\partial t} = \frac{\mathbf{T}}{Mi} \tag{19}$$

where Ma is the mass of the solid S^i, Mi its moment of inertia, ρ_{s^i} its density, ρ_f the fluid density and $\mathbf{G}$ the gravity vector. The formalism can be easily extended to multiple solids.

Table 1: Static cylinder, values of mean C_D $\left(\overline{C_D}\right)$ and St obtained at Re=150 with three different grids

h	Methods	$\overline{C_D}$	St
1/128	Noca	1.475	0.173
	Momentum	1.523	0.173
1/256	Noca	1.381	0.173
	Momentum	1.386	0.172
1/512	Noca	1.347	0.173
	Momentum	1.356	0.173

4 Numerical results

In this section, forces and moments computations are validated using a static cylinder and an oscillating flapping wing motion. Examples of fluid-solid interactions are presented to show the capabilities of the IBM.

4.1 Static cylinder test case

The computations are done on a square domain of size $[-1.85, 6.15] \times [-4, 4]$. The centre of the cylinder, whose diameter D is 0.3, is at $(0, 0)$. The far field velocity is $U_\infty = 1$. The fluid viscosity is selected to achieve the desired Reynolds number $Re = 150$. The potential flow solution around a cylinder defines reliable values of the flow field at domain boundaries. For example, on the top and bottom boundaries a Dirichlet condition is enforced. That is

$$\Psi = U_\infty y \left(1 - \frac{(D/2)^2}{x^2 + y^2}\right) \qquad \text{top, bottom.} \tag{20}$$

This is equivalent to impose a symmetry condition on top and bottom boundaries. Neumann boundary conditions are imposed at upstream and downstream locations, that is

$$\frac{\partial \Psi}{\partial x} = \frac{2U_\infty (D/2)^2 xy}{(x^2 + y^2)^2} \qquad \text{upstream, downstream.} \tag{21}$$

Three meshes with $h = 1/128$, $1/256$ and $h = 1/512$, where h is the grid spacing, are used for computations. The time step dt for computation is evaluated by

$$dt = (0.5h)^2 Re \tag{22}$$

where the Reynolds number is defined as $Re = U_\infty D/\nu$.

Table 1 compares some results obtained with the three meshes to evaluate grid sensitivities of the results. The forces F_x and F_y are obtained with the Noca formulation [31] and Momentum formulation equation (15). The mean drag coefficient $\overline{C_D}$, C_X averaged over one period and the Strouhal number St are tabulated. The St value depends on the shedding frequency f or on the dimensionless time period T_p

$$St = \frac{fD}{U_\infty} = 1/T_p \,.$$

The dimensionless time period is evaluated by looking at the lift coefficient, C_Y, evolution in time. For three significant digits, the St values do not depend on the force formulation or on the mesh size. It is expected that for a fine enough mesh, the two formulations should give the same results. The average mean drag coefficient values are between the values of 1.44 from Lai and Peskin [43] and 1.334 from Liu *al.* [44]. The Strouhal number are close to the value of 0.184 computed in [43].

4.2 Validation of forces through an oscillating airfoil

Flapping wing motions are extensively studied for engineering applications in low Reynolds numbers flow where classical fixed wing geometry performance decreases, [45]. According to previous works, around ten parameters influence the power extraction in flapping wing motions, such as oscillation frequencies and amplitudes (translational and rotational), phase difference between plunge and pitch motion, viscosity, free stream velocity, flapping pattern and airfoil geometry. In this section, we will study the effect of the pitching position and of the geometry's shape, after the validation of unsteady forces calculations.

For validation, an oscillating airfoil experiencing simultaneous pitching $\theta(t)$ and heaving $h(t)$ motions is modelled. The infinitely long wing is based on a NACA 0015 airfoil. The pitching axis is located along the airfoil chord at the position $(x_p, y_p) = (1/3, 0)$. The airfoil motion, described by Kinsey and Dumas [46], is defined by the heaving $h(t)$ and the pitching angle $\theta(t)$ as follows

$$\begin{cases} h(t) = H_0 \sin(\omega t + \Phi) \\ \theta(t) = \theta_0 \sin(\omega t) \end{cases} \tag{23}$$

where H_0 is the heaving amplitude and θ_0 is the pitching amplitude. The angular frequency is defined by $\omega = 2\pi f$ and the phase difference Φ is set to 90°. The heaving velocity is then given by

$$V_y(t) = H_0 \omega \cos(\omega t + \Phi). \tag{24}$$

Based on the imposed motion and on the upstream flow conditions, the airfoil experiences an effective angle of attack $\alpha(t)$ and an effective upstream velocity $V_{eff}(t)$ defined by

$$\begin{cases} \alpha(t) = \arctan(-V_y(t)/U_\infty) - \theta(t) \\ V_{eff}(t) = \sqrt{\left(U_\infty^2 + V_y^2(t)\right)}, \end{cases} \tag{25}$$

where the freestream velocity far upstream of the oscillating airfoil is $U_\infty = 1$.

To validate our simulations, a regime corresponding to the parameters $Re = \dfrac{U_\infty c}{\nu} = 1100$, $H_0/c = 1$, $f = 0.14$, $x_p/c = 1/3$ and $\theta_0 = 76.33^o$ has been computed. A view of the motion is sketched in figure 4. Our numerical results, obtained using $dx = dy = 1 \times 10^{-3}$, $dt = 5 \times 10^{-4}$ and $\lambda = 1 \times 10^8$, are then compared to the forces predictions presented by Kinsey et al. [46] and by Campobasso et al. [47]. Results of instantaneous forces, equation (17), C_X, C_Y and pitching moments C_m, figure 5, are in good agreements with literature results. Our solution slightly overestimates the drag coefficient amplitude and the minimum/maximum of the lift coefficient but correctly predicts the curve shape of those coefficients. The momentum coefficient is correctly predicted as well, our curve is slightly shifted to the left compared to literature results (corresponding to a time lag), figure (5c).
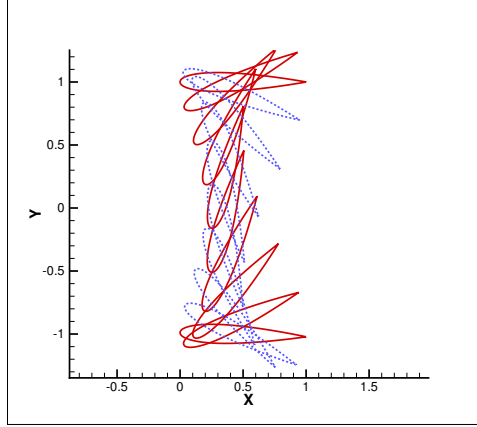
Figure 4: Oscillating airfoil, sketch of the airfoil motion for $H_0/c = 1$, $f = 0.14$, $x_p/c = 1/3$ and $\theta_0 = 76.33^o$.

A mesh sensitivity study using different mesh sizes and different domain sizes has been performed to verify the sensibility of the force predictions. All the simulations used the same time step fixed to $dt = 5 \times 10^{-4}$. Figures 6 (a), (b) and (c) compare C_X, C_Y and C_m obtained with three different meshes corresponding to a coarse mesh $dx = dy = 5 \times 10^{-3}$, a medium mesh $dx = dy = 2 \times 10^{-3}$ and a fine mesh $dx = dy = 1 \times 10^{-3}$ and demonstrate the consistency of the method. Each mesh allows to compute a good approximation of the forces and moment evolution through a time period. As the mesh becomes finer the solution converges to the solution obtained on the finest mesh.

Simulations using the medium grid scale $dx = dy = 2 \times 10^{-3}$ and two different domains, one domain of size $[-3, 8] \times [-4, 4]$ referenced as dom1 and the other one of size $[-3, 8] \times [-6, 6]$ referenced as dom2, have also been performed to investigate boundary conditions effects and more especially blocking effects on the solution. Figure 6 (d) demonstrates that a small blocking effect is observable on this test case. Indeed, reducing slightly the height of the domain leads to an amplitude increase of the C_X coefficient. Since the comparisons with the literature results have been done on the smallest domain, the blocking effects are most probably responsible of the overestimation noticed on the C_X curve. However, even the coarse mesh on the small domain exhibits the correct behavior of the solution. The following studies are then performed using the smallest domain and the medium grid scale to ensure a good compromise between the quality of the solution and cpu time.

4.3   Flexibility offered by penalization

Penalization technique offers a simple way to consider different geometries for the solid S^i because the same mesh can be used for all simulations. To illustrate this capability of the method three kind of geometries have been selected. The NACA 0015 profile, a rounded edge rectangular plate with a ratio chord/thickness = 15% and a NACA 0040 profile. Those geometries are sketched on figure (7a). The method enables also to easily modify the position of the pitching axis, thus two different positions have been selected $(x_p, y_p) = (1/3, 0)$ and $(x_p, y_p) = (1/2, 0)$. Those geometries evolve using the same motion as described in section 4.2.

For the first position of the pitching axis $(1/3, 0)$, the motion of tow of the three geometries is sketched on figures 4 & 7(b). Figure (8) compares C_X, C_Y and C_m for the three geometries.
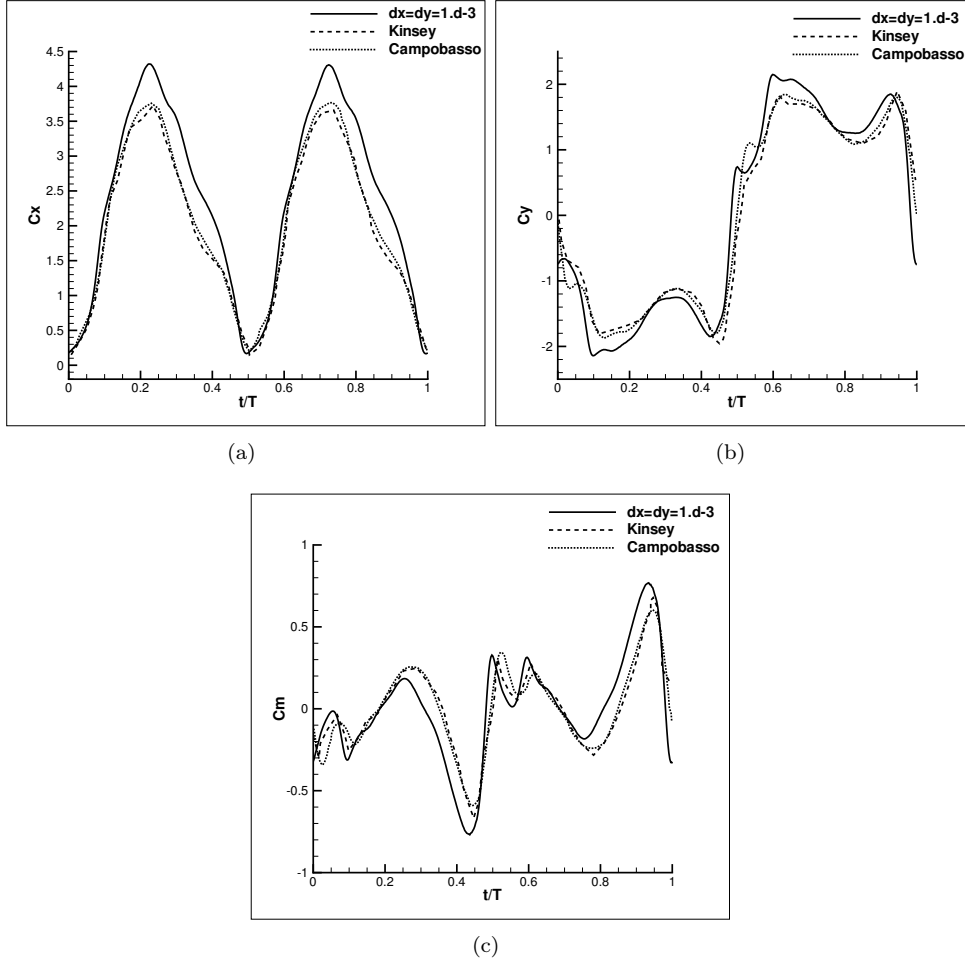
Figure 5: Oscillating airfoil, comparison with the results obtained by Kinsey et al.[46] and Campobasso et al. [47] (a) Drag coefficient, (b) Lift coefficient, (c) Pitching moment.

As expected for such a low Reynolds number flow the results obtained with the NACA 0015 airfoil and the rectangular plate of the same thickness are very similar. The thicker airfoil on the contrary exhibits a different behavior. As in the work done by Ashraf *al.* [48], depending on the Reynolds number, flow around thicker flapping airfoils can be radically different than flow around thin geometries. Indeed, results of the mean power, table (2), show that thin geometries extract 1.5 to 3 times more power than thick geometry. The instantaneous power results from the sum of the heaving contribution $\mathbf{F}_y V_y(t)$ and the pitching contribution $\mathbf{T}\dot{\theta}(t)$, where $\mathbf{T}$ is the resulting torque about the pitching axis x_p. The mean power extracted over one cycle can thus be computed using equation (26).

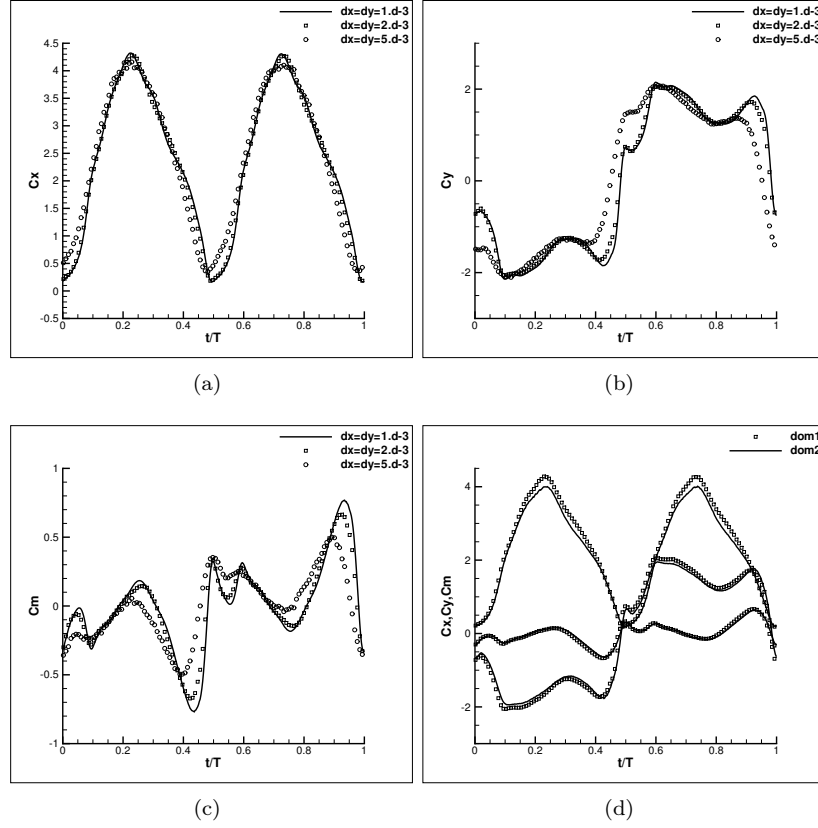$$C_{power} = \frac{P_{power}}{\frac{1}{2}\rho U_\infty^3 c}$$

Figure 6: Mesh sensitivity on the drag coefficient (a) on the lift coefficient (b) and on the pitching moment (c). For the medium mesh, $dx = dy = 2 \times 10^{-3}$ influence of the domain size on calculated forces and moment, dom1 $= [-3, 8] \times [-4, 4]$, dom2$=[-3, 8] \times [-6, 6]$.

$$\overline{C_{power}} = \int_0^1 \left(C_Y(t) \frac{V_y(t)}{U_\infty} + C_m(t) \frac{\dot{\theta}(t)c}{U_\infty} \right) dt. \tag{26}$$

Moving the pitching position from the leading edge to the middle of the wing increases the mean power extracted for the thick airfoil and on the contrary decreases the mean power for thin geometries, table 2.

The results related to the motion corresponding to the second pitching axis location $(x_p, y_p) = (1/2, 0)$ are presented in figures (10) and (11). First, the motion using this pitching axis loaction is sketched in figure (9). Figure (10) compares the evolution over one cycle of C_X, C_Y and C_m for the three geometries. Again the NACA 0015 airfoil and the rectangular plate exhibit comparable behaviors, the curves evolving with a similar pattern. The thick airfoil results remain different.

The modification of the pitching axis position reduces the C_X coefficient for the three geometries, figures (11a-d-g). The pitching moment coefficient become antisymmetric as expected thanks to the symmetry of the motion, figures (11c-f-i). For thin geometries, the modification of the pitching location leads to related modification of the curves. C_X, C_Y and C_m curves from

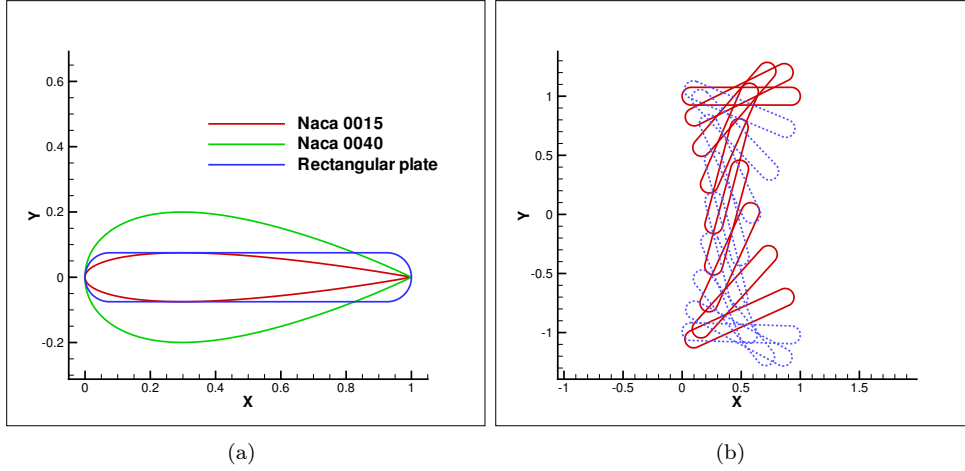(a)   (b)

Figure 7: a) Geometries of the NACA 0015 profile, NACA 0040 profile and the rectangular plate. b) Motion of the rectangular plate for a pitching position at $x_p = 1/3, y_p = 0$.

Table 2: Mean C_{power} for the three geometries and the two axis pitching position

Geometry	$(x_p, y_p) = (1/3, 0)$	$(x_p, y_p) = (1/2, 0)$
NACA 0015	0.945	0.830
NACA 0040	0.339	0.625
Rectangular plate	1.043	0.830

figures (11a and d), (b and e) and (c and f) respectively look similar. The flow around the thick airfoil seems more affected by the position of the pitching axis, figures(11g-h-i).

4.4   Fluid-solid interaction

In this sub-section, trajectories of objects are computed using the proposed fluid-solid interaction model. We will first validate our model against a 2D falling cylinder to compare with literature results. Then we will use the rectangular plate described previously to study the effects of density ratios on the trajectories.

4.4.1   Falling cylinder

This test case is representative of the sedimentation of a 2D cylinder on a flat plate. We consider the case of a 2D cylinder in a square cavity, falling under gravity on a flat plane. The dimension of the cavity is $[0, 2] \times [0, 6]$. The viscosity is 0.01. The density inside and outside the cylinder is, respectively, 1.5 and 1. The mesh spacing is $dx = dy = 3.9 \times 10^{-3}$. The cylinder has a radius of 0.125, no roughness, and its barycenter is initially located at the point (1,4). To impose wall boundary conditions on each wall of the cavity we use a penalization layer of 10 cells all around the cavity, this is the reason why the domain, in figure (12a) appears slightly larger and longer than the cavity definition. A snapshot of the vorticity field, at time $t = 0.3$, is depicted in figure
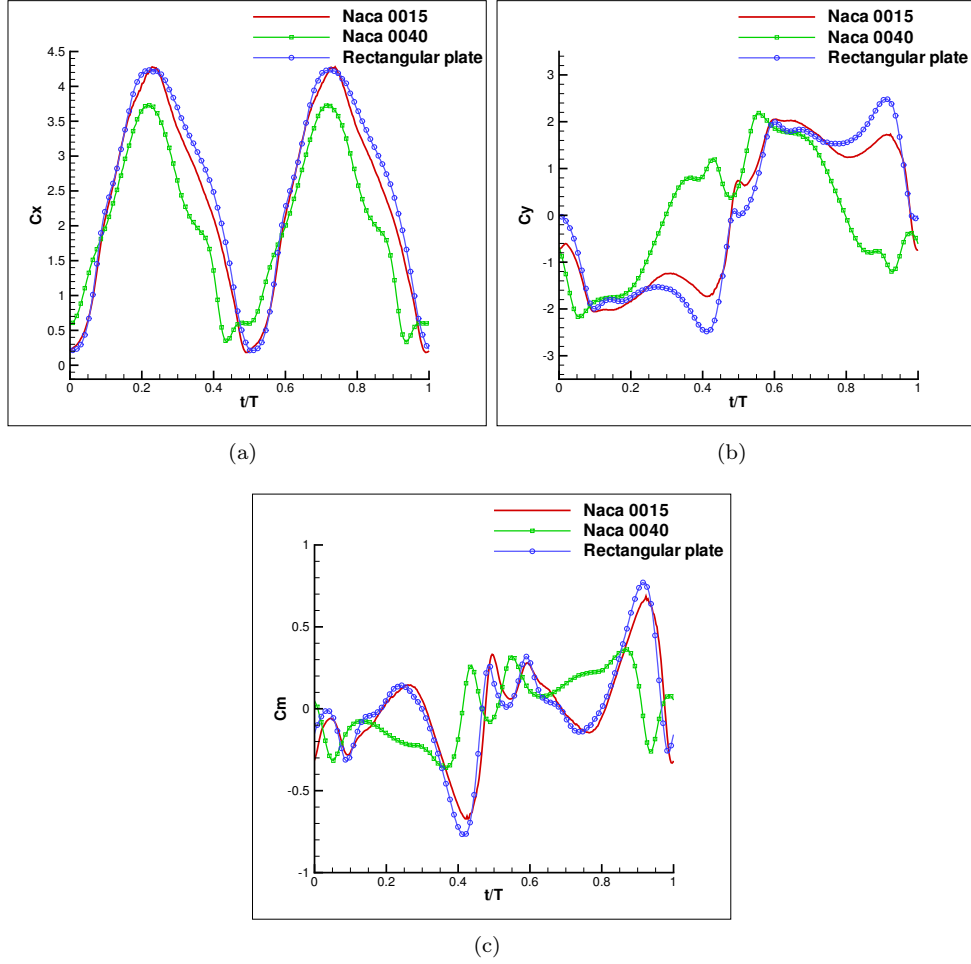
(a)

(b)

(c)

Figure 8: (a) C_X, (b) C_Y, (c) Cm corresponding to the 3 geometries for a pitching axis at $x_p = 1/3$, $y_p = 0$.

(12a). The vorticity along the cavity walls results from blocking effects. The falling cylinder creates an upward flow to satisfy the mass conservation. The cylinder accelerates under gravity, set to $g = -980$, then stabilizes its velocity around a steady velocity, due to equilibrium between friction forces, buoyancy and gravity. Then it hits the bottom of the cavity and bounces, figure (12b). Information on the collision model used can be found in [49], the parameters chosen for the linear spring collision model are the Young modulus set to $E = 1.083e9$, the Poisson's coefficient set to 0.8235 and the friction coefficient set to 0.1. The evolution of the vertical velocity component v as a function of time is plotted in figure (12) and is in agreement with the solution of Coquerelle *et al.* [24]. The influence of the time step on the vertical velocity is also presented in this figure showing the consistency of the model to simulate the physical phenomenon.
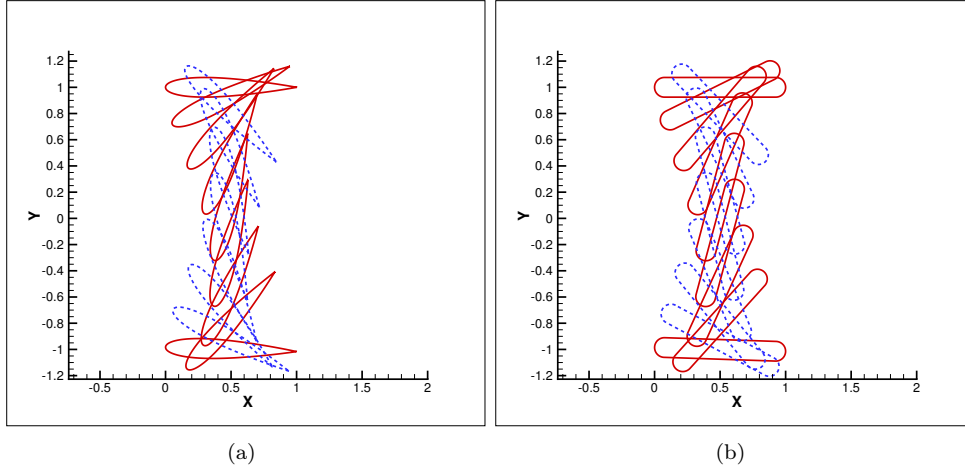
Figure 9: Motion of the geometries for a pitching position at $x_p = 1/2, y_p = 0$.

4.4.2 Falling rectangular plate

We use the previous rectangular plate, from sub-section 4.3 for which the gravity center of the plate is positionned at $(0,0)$ with a rotation angle of attack of $\pi/3$ with the horizontal axis, the computational domain is set to $[-3, 8] \times [-4, 4]$. First we compute the flow motion around the fixed rectangular plate. The Reynolds number is set at $Re = 1100$ as in the previous study using this solid body, see section 4.3. A snapshot of the vorticity field around the fixed plate is presented in figure (13). At time $t = 0.5$, the fluid-solid interaction is started. Once the fluid-solid interaction occurs, the aerodynamic forces and moment acting on the solid induce its motion. During these simulations, the pivot axis of the rectangular plate coincides with its barycenter. The first simulations consist in investigating the sensitivity of the trajectory according to the mesh. In those simulations $\rho_s = \rho_f$ and the time step dt is fixed to 5×10^{-4}. Figure (14a) presents the position of the plate every 400 steps using 5 meshes. The plate trajectory is very stable according to the grid size. As can be seen through figures (14b-d) the evolution in time of the velocities (u-component, v-component and angular velocity) is similar. The velocities value evolves smoothly from the coarser mesh to the finer mesh. The angle of rotation with the initial position, figure (14d) induce a similar motion of the plate for all the meshes. The range of the trajectory and the reactivity of the rectangular plate to the flow is slightly affected by the grid size.

To verify the influence of plate's density on the trajectory, four density ratios have been selected $\rho_s/\rho_f = 2$; 1.75; 1.5 and 1.25. The simulations have been performed using the medium mesh $dx = dy = 3. \times 10^{-3}$ with a time step of $dt = 5 \times 10^{-4}$ and a domain of $[-3, 5] \times [-9, 3]$. As expected, from previous work in literature [35], the plate starts to auto-rotate, figure (15a). The auto-rotation starts sooner for larger density ratio. Again, figure (15a), shows the position of the plate every 400 time steps for each density ratio. The falling velocity, v (figure 15d), of the plate increases with the plate weight. The vertical acceleration of the plate destabilizes its orientation and the plate starts to rotate around its barycenter axis, figure (15e). The modification of the plate orientation with the flow reduces the falling velocity (the gravity force is compensated by buoyancy and aerodynamic forces), figure (15d). Due to its initial orientation and its weight, at the beginning of the fluid-solid interaction, the plate glides to the left (figures 15b & c). As expected, the lighter plate is more affected by the flow and is pushed to the right by the flow.
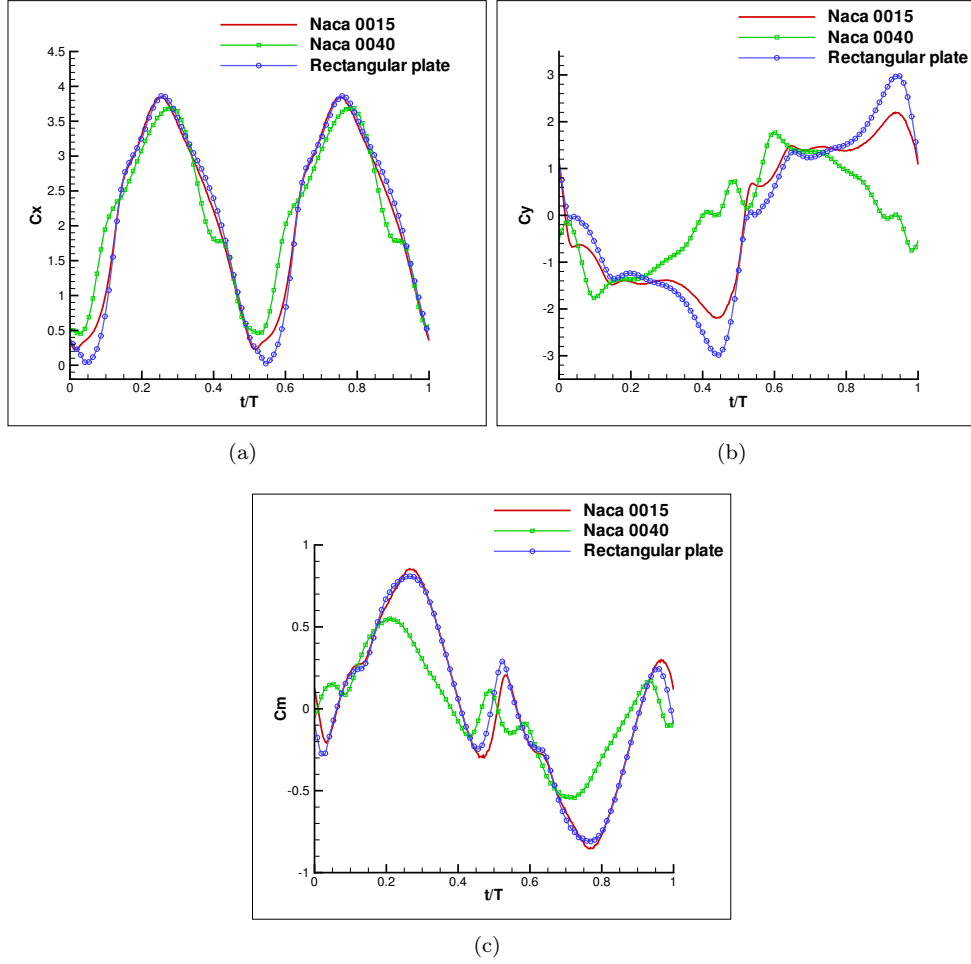
Figure 10: (a) C_X, (b) C_Y, (c) Cm corresponding to the 3 geometries for a pitching position at $x_p = 1/2$, $y_p = 0$.

For the cylinder and the rectangular plate test cases the fluid-solid interaction model behaves consistently for varying density ratio, mesh size and time step.

5   Conclusions

This paper has presented an original way of computing aerodynamic forces and moments along with the governing equations to use them in order to simulate fluid-solid interactions. Forces and moments have been validated within the VIC-IBM scheme using static and dynamic bodies. Predicted forces and moment agree with literature for a static cylinder and a flapping wing motion. The flexibility offered by the use of IBM and the level-set description of the geometries has been demonstrated. The fluid-solid interaction model has been compared to another approach for a falling cylinder test case and the falling velocity agrees with literature results. For varying
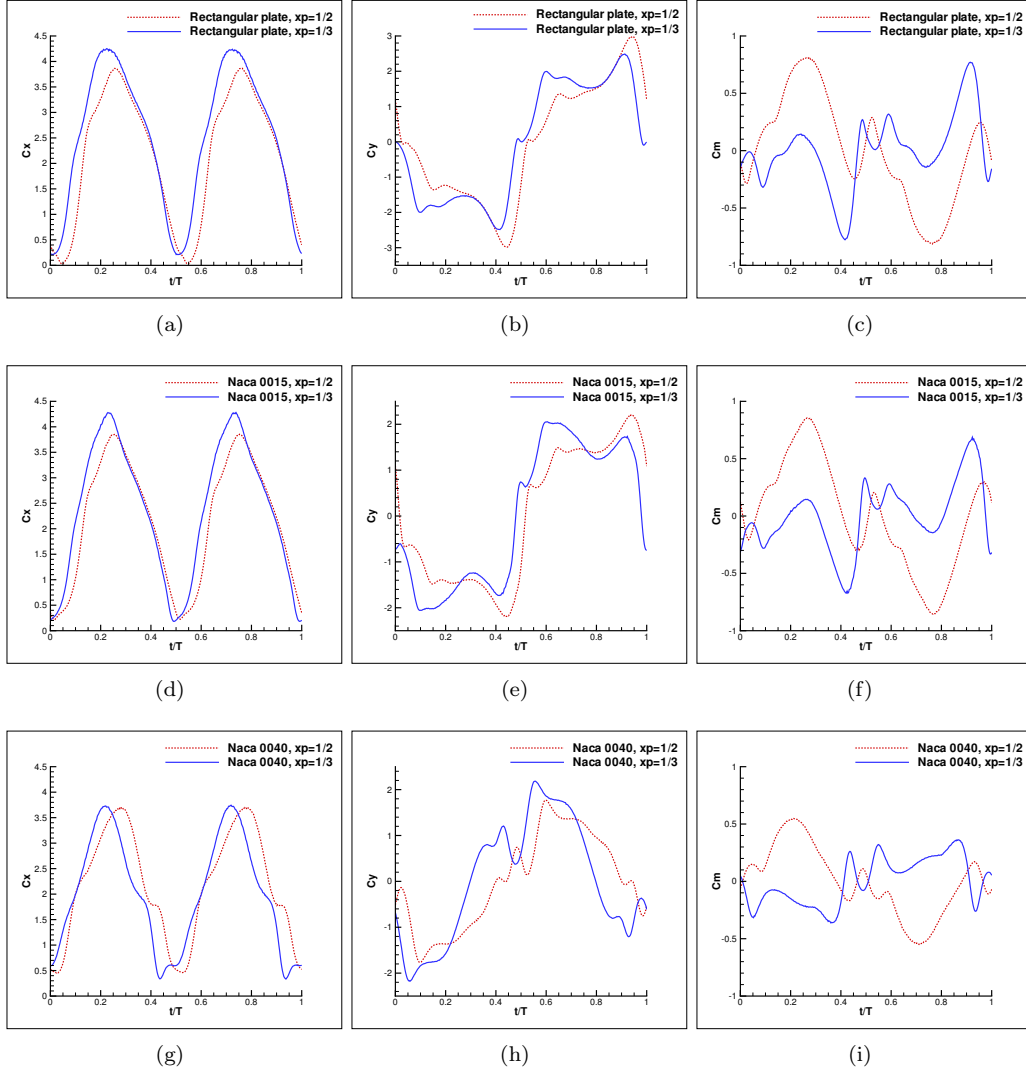
Figure 11: Pitching axis position comparison (a-b-c) plate, (d-e-f) NACA 0015, (g-h-i) NACA 0040.

density ratio, mesh size and time step, the fluid-solid interaction model predicts realistic trajectories for a rectangular plate. Further experimental results are needed to properly validate this model. Since aeronautic applications will be considered with the computation of ice shedding trajectories a specific turbulent wall model is under development.
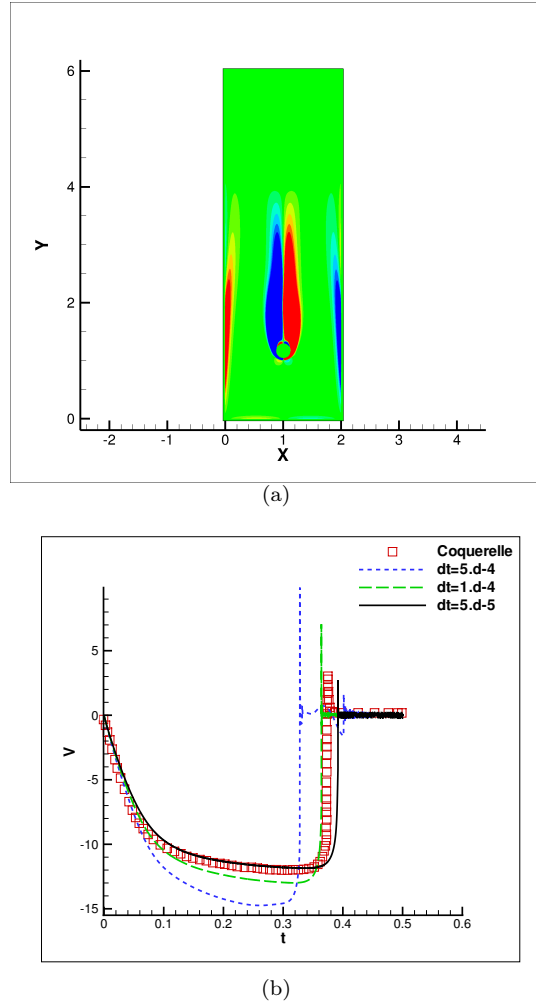
6 Ackowledgement

(a)

(b)

Figure 12: Sedimentation of a 2D falling cylinder. a) Vorticity field at time $t = 0.3$. b) Sensitivity of the solution against the time step and comparison against Coquerelle's velocity profile [24] .

References

References

[1] R. Mittal, G. Iaccarino, Immersed boundary methods, Annu. Rev. Fluid. Mech. 37 (2005) 239–261.

[2] J. T. Rasmussen, G. H. Cottet, J. H. Walther, A multiresolution remeshed vortex-in-cell algorithm using patches, Journal of Computational Physics 230 (2011) 6742–6755.
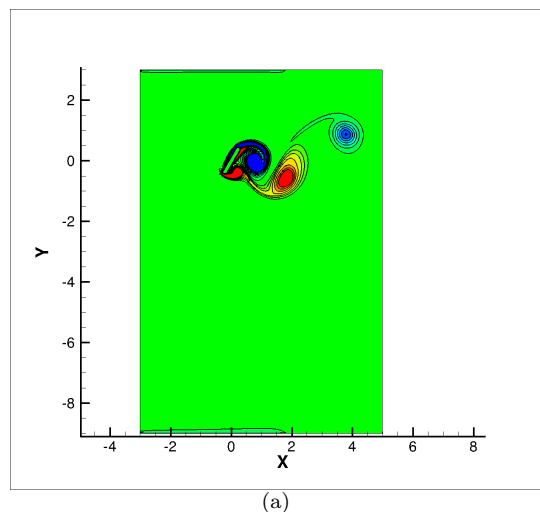
(a)

Figure 13: Solution around the static rectangular plate, vorticity contours (negative in blue; positive in red).

[3] F. Capizzano, Turbulent wall model for immersed boundary methods, AIAA Journal 49 (11).

[4] R. Ghias, R. Mittal, H. Dong, A sharp interface immersed boundary method for compressible viscous flows, Journal of Computational Physics 225 (2007) 528–553.

[5] F. Capizzano, E. Iuliano, A eulerian method for water droplet impingement by means of an immersed boundary technique, Journal of Fluids Engineering-Transactions of the Asme 136 (4).

[6] F. Sotiropoulos, X. L. Yang, Immersed boundary methods for simulating fluid-structure interaction, Progress in Aerospace Sciences 65 (2014) 1–21.

[7] F. Tseng, A ghost cell immersed boundary method for flow in complex geometry, Journal of Computational Physics 192 (2003) 593–623.

[8] Y. Gorsse, A. Iollo, H. Telib, L. Weynans, A simple second order cartesian scheme for compressible euler flows, Journal of Computational Physics 231 (2012) 7780–7794.

[9] A. Sarthou, S. Vincent, P. Angot, J. Caltagirone, The sub-mesh penalty method, Finite Vol. Complex Appl. V (2008) 633–640.

[10] M. Linnick, H. Fasel, A high order interface method for simulating unsteady incompressible flows on irregular domains, Journal of Computational Physics 204 (2005) 157–192.

[11] P. Collela, D. Graves, B. Keen, D. Modiano, A cartesian grid embedded boundary method for hyperbolic conservation laws, Journal of Computational Physics 211 (2006) 347–366.

[12] P. Angot, C. Bruneau, P. Fabrie, A penalization method to take into account obstacles in incompressible viscous flows, Numerische Mathematik 81 (4) (1999) 497–520.

[13] E. Arquis, J. Caltagirone, Sur les conditions hydrodynamiques au voisinage d'une interface milieu fluide-milieux poreux: application à la convection naturelle, C.R. Acad. Sci. Paris II 299 (1984) 1–4.

[14] M. Bergmann, A. Iollo, Modeling and simulation of fish-like swimming, Journal of Computational Physics 230 (2) (2011) 329–348.

[15] O. Boiron, G. Chiavassa, R. Donat, A high-resolution penalization method for large mach number flows in the presence of obstacles, Comput. Fluids 38 (3) (2009) 703–714.

[16] R. Abgrall, H. Beaugendre, C. Dobrzynski, An immersed boundary method using unstructured anisotropic mesh adaptation combined with level-sets and penalization techniques, Journal of Computational Physics 257 (2014) 83–101.

[17] B. Kadoch, D. Kolomenskiy, P. Angot, K. Schneider, A volume penalization method for incompressible flows and scalar advection-diffusion with moving obstacle, Journal of Computational Physics 231 (2012) 4365–4383.

[18] F. Morency, H. Beaugendre, F. Gallizio, Aerodynamic force evaluation for ice shedding phenomenon using vortex in cell scheme, penalisation and level set approaches, International Journal of Computational Fluid Dynamics 26 (9-10) (2012) 435–450.

[19] P. Koumoutsakos, A. Leonard, High-resolution simulations of the flow around an impulsive started cylinder using vortex methods, Journal of Fluid Mechanics 296 (1995) 1–38.

[20] P. Ploumhans, G. S. Winckelmans, J. K. Salmon, A. Leonard, M. S. Warren, Vortex methods for direct numerical simulation of three-dimensional bluff body flows: application to the sphere at re = 300, 500, and 1000, Journal of Computational Physics 178 (2) (2002) 427–463.

[21] G. Cottet, P. Koumoutsakos, Vortex methods: theory and practice, Cambridge Univ Pr, 2000.

[22] G. Cottet, P. Poncet, Advances in direct numerical simulation of 3d wall-bounded flows by vortex-in-cell methods, Journal of Computational Physics 193 (2003) 136–158.

[23] N. Kevlahan, J. Ghidaglia, Computation of turbulent flow past an array of cylinders using a spectral method with brinkman penalization, Eur. J. Mech. B20 (2001) 333–350.

[24] M. Coquerelle, G. Cottet, A vortex level set method for the two-way coupling of an incompressible fluid with colliding rigid bodies, Journal of Computational Physics 227 (21) (2008) 9121–9137.

[25] C. Mimeau, I. Mortazavi, G. Cottet, Passive flow control around a semi-circular cylinder using porous coatings, Int. Journal of flow control 6 (1) (2014) 43–60.

[26] C. Mimeau, F. Gallizio, G. Cottet, I. Mortazavi, Vortex penalization method for bluff body flows, submitted to Int. Jour. for Num. Meth. in Fluids.

[27] M. Gazzola, B. Hejazialhosseini, P. Koumoutsakos, Reinforcement learning and wevelet adapted vortex methods for simualtions of self-propelled swimmers, SIAM J. Sci. Comput. 36 (3) (2014) B622–B639.

[28] G. Cottet, J.-M. Etancelin, F. Perignon, C. Picard, High order semi-lagrangian particles for transport equations : numerical analysis and implementation issues, ESAIM: Mathematical Modelling and Numerical Analysis 48 (2014) 1029–1064.

[29] J. Rasmussen, G. Cottet, J. Waltherw, A multiresolution remeshed vortex-in-cell algorithm using patches, Journal of Computational Physics 230 (2011) 6742–6755.

[30] D. Rossinelli, M. bergdof, G. Cottet, P. Koumoutsakos, Gpu accelerated simulations of bluff body flows using vortex particle methods, Journal of Computational Physics 229 (2010) 3316–3333.

[31] F. Noca, D. Shiels, D. Jeon, A comparison of methods for evaluating time-dependent fluid dynamic forces on bodies, using only velocity fields and their derivatives, Journal of Fluids and Structures 13.

[32] M. Pocwierz, A. Styczek, Calculation of the force on solid body in the unsteady flow of incompressible fluid, Archives of Mechanics 62 (2) (2010) 103–19.

[33] J. D. Eldredge, Dynamically coupled fluid-body interactions in vorticity-based numerical simulations, Journal of Computational Physics 227 (21) (2008) 9170–94. `doi:10.1016/j.jcp.2008.03.033`.

[34] X. Q. Zhang, P. Theissen, J. U. Schlüter, Towards simulation of flapping wings using immersed boundary method, International Journal for Numerical Methods in Fluids 71 (2013) 522–536.

[35] R. Mittal, V. Seshadri, H. S. Udaykumar, Flutter, tumble and vortex induced autorotation, Theoretical and Computational Fluid Dynamics 17 (3) (2004) 165–170.

[36] R. Glowinski, T. W. Pan, T. I. Hesla, D. D. Joseph, J. Périaux, A fictitious domain approach to the direct numerical simulation of incompressible viscous flow past moving rigid bodies: Application to particulate flow, Journal of Computational Physics 169 (2) (2001) 363–426.

[37] S. Bonisch, V. Heuveline, On the numerical simulation of the unsteady free fall of a solid in a fluid: I. the newtonian case, Computers and Fluids 36 (9) (2007) 1434–1445. `doi:10.1016/j.compfluid.2007.01.010`.

[38] P. R. Andronov, D. A. Grigorenko, S. V. Guvernyuk, G. Y. Dynnikova, Numerical simulation of plate autorotation in a viscous fluid flow, Fluid Dynamics 42 (5) (2007) 719–31. `doi:10.1134/S0015462807050055`.

[39] D. M. Hargreaves, B. Kakimpa, J. S. Owen, The computational fluid dynamics modelling of the autorotation of square, flat plates, Journal of Fluids and Structures 46 (2014) 111–33. `doi:10.1016/j.jfluidstructs.2013.12.006`.

[40] G. Cottet, B. Michaux, S. Ossia, G. VanderLinden, A comparison of spectral and vortex methods in three-dimensional incompressible flows, Journal of Computational Physics 175 (2) (2002) 702–712.

[41] J. Monaghan, Extrapolating B splines for interpolation, Journal of Computational Physics 60 (2) (1985) 253–262.

[42] H. Beaugendre, F. Morency, F. Gallizio, S. Laurens, Computation of ice shedding trajectories using cartesian grids, penalization, and level sets, Modelling and Simulation in Engineering 2011 (2011) 1–15.

[43] M. Lai, C. Peskin, An immersed boundary method with formal second-order accuracy and reduced numerical viscosity, Journal of Computational Physics 60 (2000) 705–719.

[44] C. Liu, X. Zheng, C. Sung, Preconditioned multigrid methods for unsteady incompressible flows, Journal of Computational Physics 139 (1) (1998) 35Ð57.

[45] H. Gopalan, A. Povitsky, Lift enhancement of flapping airfoils by generalized pitching motion, Journal of Aircraft 47 (6) (2010) 1884–1897. `doi:Doi10.2514/1.47219`.

[46] T. Kinsey, G. Dumas, Parametric study of an oscillating airfoil n a power-extraction regime, AIAA Journal 46 (6) (2008) 543–561.

[47] M. S. Campobasso, J. Drofelnik, Compressible navier-stokes analysis of an oscillating wing in a power-extraction regime using efficient low-speed preconditioning, Computers & Fluids 67 (2012) 26–40.

[48] M. A. Ashraf, J. Young, J. C. S. Lai, Reynolds number, thickness and camber effects on flapping airfoil propulsion, Journal of Fluids and Structures 27 (2) (2011) 145–160. `doi:10.1016/j.jfluidstructs.2010.11.010`.

[49] F. Morency, H. Beaugendre, R. Dufrénot, Mathematical model for ice wall interactions within a level set method, in: proceedings for the 49th International Symposium of Applied Aerodynamics 3AF, 2014.
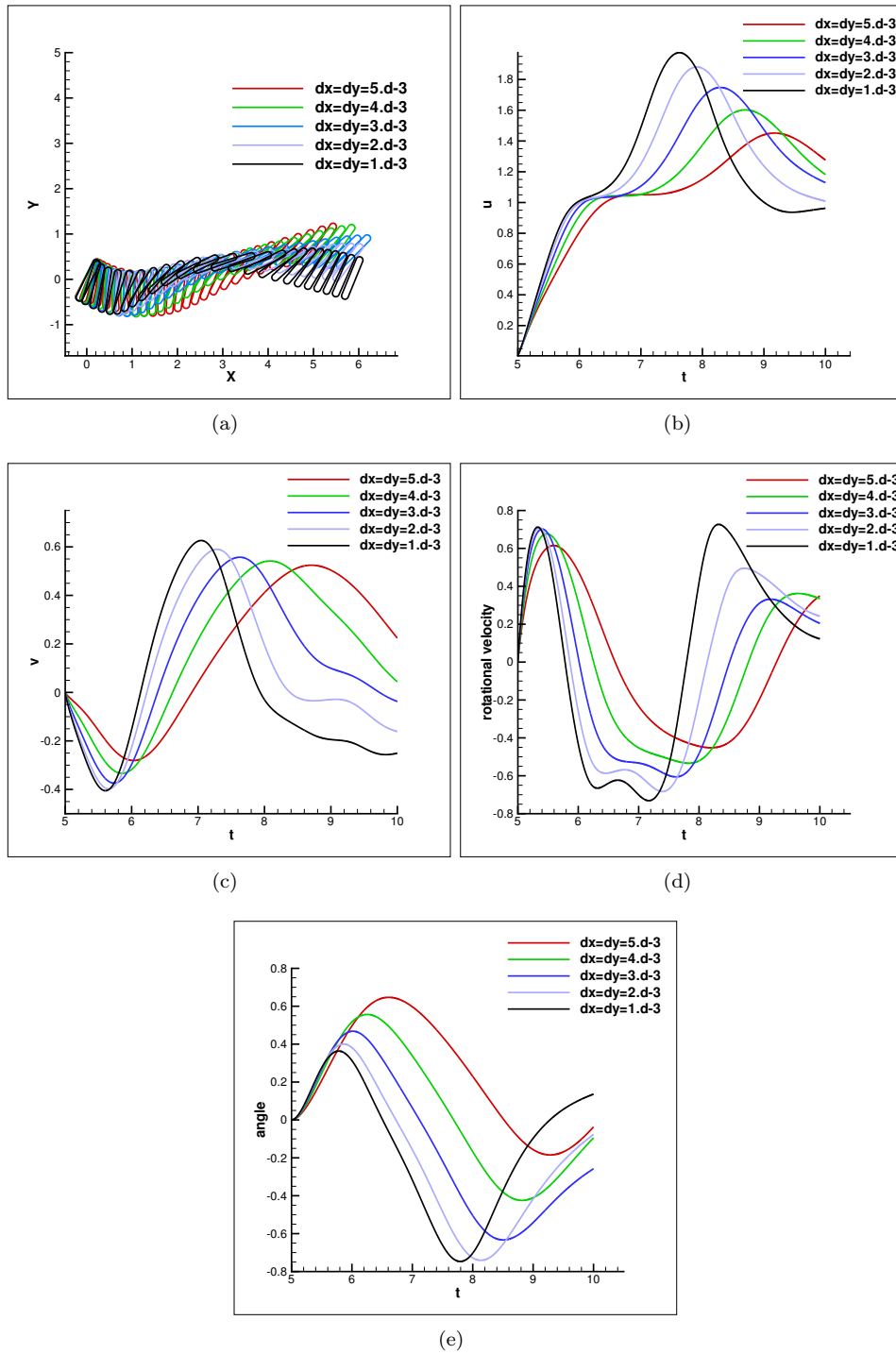
Figure 14: Grid sensitivity study on the rectangular plate trajectories: (a) position of the plate along the trajectories; (b) evolution of u-velocity component (c) evolution of v-velocity component (d) evolution of the angular velocity and (e) evolution of the rotational angle.
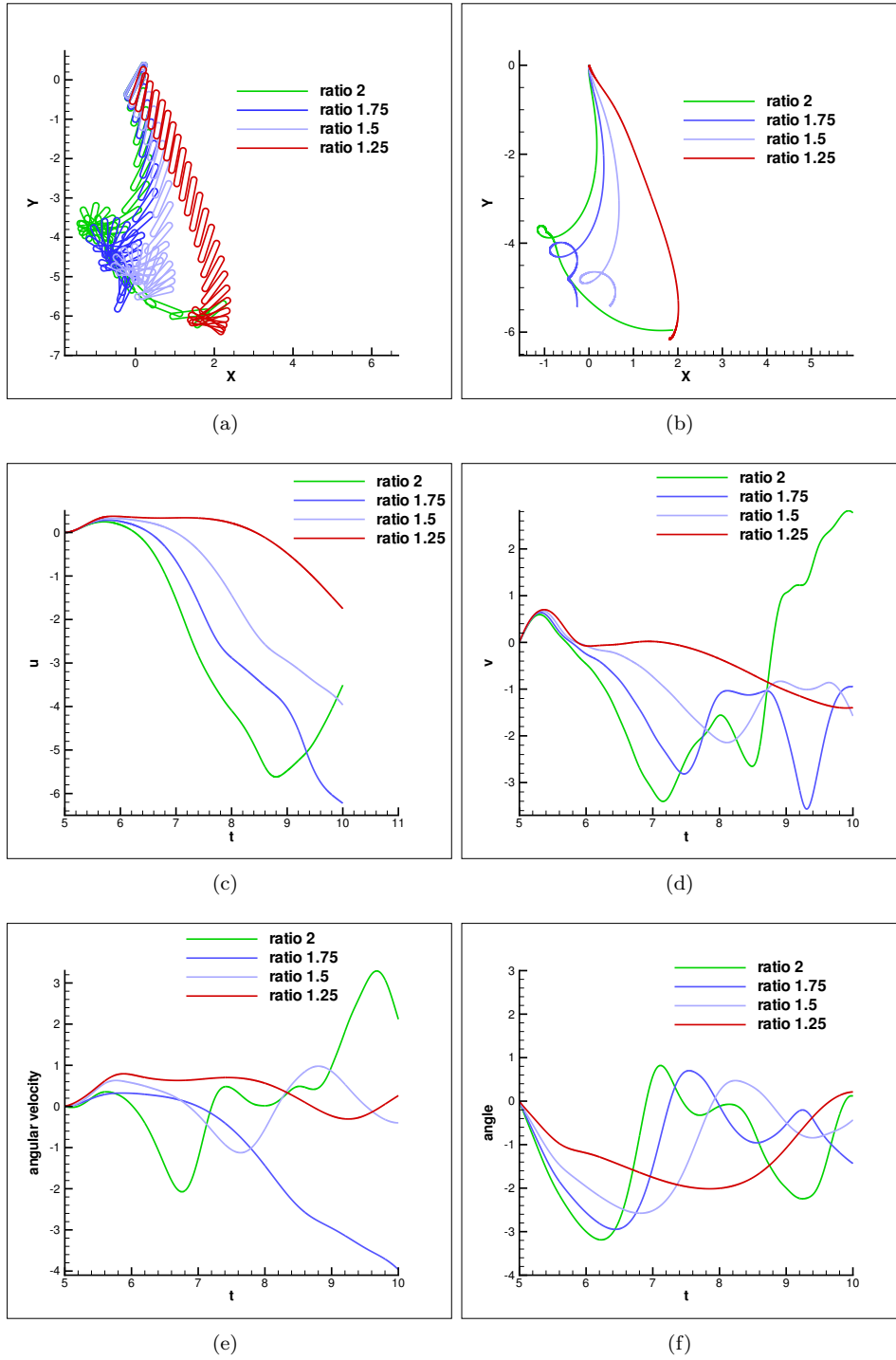
Figure 15: Density investigation, the solid-fluid interaction starts at $t = 5$, mesh size $h = 3 \times 10^{-3}$ (a) trajectories; (b) position of barycenter; (c) u-velocity; (d) v-velocity; (e) angular-velocity; (f) angle.